Available online at www.sciencedirect.com
ScienceDirect
International Journal of Heat and Fluid Flow 28 (2007) 542–551
International Journal of HEAT AND FLUID FLOW
www.elsevier.com/locate/ijhff

Direct numerical simulation of bubbly flow in the turbulent boundary layer of a horizontal parallel plate electrochemical reactor

Thomas Nierhaus *, David Vanden Abeele, Herman Deconinck

Von Karman Institute for Fluid Dynamics, Aeronautics and Aerospace Department, Waterloose Steenweg 72, B-1640 St-Genesius-Rode, Belgium

Received 6 November 2006; received in revised form 8 March 2007; accepted 29 March 2007
Available online 21 May 2007

Abstract

We perform direct numerical simulation (DNS) of a turbulent bubble-laden channel flow of shear Reynolds number $Re_\tau = 131$ to analyse mass transfer in a parallel plate electrochemical reactor. We set aside the electrochemical part of the problem and focus on the simulation of a turbulent channel flow of a liquid electrolyte with gas bubbles evolving from an electrode located at the bottom wall of the channel. We use an Eulerian–Lagrangian representation to simulate dispersed two-phase flow, where two-way momentum coupling between the bubbles and the electrolyte is taken into account. Three-dimensional simulations are obtained using a distributed memory parallel computer architecture. Investigations on the bubble motion due to advection and gravitational rise are carried out and the interaction of bubbles with turbulent flow structures is analysed. Furthermore, the role of the lift force acting on the bubbles is investigated. Mean volume fraction statistics are shown for validation purposes. An analysis of instantaneous flow fields and bubble distributions as well as order-of-magnitude analyses are used to determine which forces are mostly influencing the bubble dynamics and dispersion.

Keywords: Bubbly flow; Direct numerical simulation; Electrochemical reactor; Eulerian–Lagrangian model; Lift force; Turbulent flow; Two-phase flow

1. Introduction

Turbulent bubble-laden flows occur in a wide variety of industrially relevant processes. One example of such a process is electrochemical graining. In this technique, a peak and valley structure is etched into the surface of a metallic electrode by means of chemical reactions between the surface material and an acidic electrolyte.

We perform DNS of turbulent bubble-laden flow to analyse the mass transfer in a parallel plate reactor, which is a simplified electrochemical experimental device approximating existing industrial set-ups for electrochemical graining. A simple sketch of such a device is shown in Fig. 1. Basically, the parallel plate reactor features turbulent flow of an electrolyte in a channel with a cathode at the bottom and an anode at the top. An externally applied potential difference causes ion migration in the electrolyte and electrochemical reactions at the electrodes. Due to those reactions, gas bubbles can be formed at nucleation sites on the electrode surfaces. Those bubbles grow and detach from the electrode into the flow, where they are carried away by the electrolyte and experience a rise due to buoyancy.

Typical sizes of bubbles formed in electrochemical reactions are in the micrometer regime. Due to their small diameters, they are of low Weber number, meaning that they are spherical and their dynamics can be assumed to be independent of their surface tension. Therefore, we generally assume the bubbles in our frame of interest to be of spherical shape and non-deformable. Also, small spherical bubbles have a very low tendency of breaking up due to their high surface tension. Therefore, we neglect bubble break-up in the present work.

From the theory of turbulent flows, it is known that the energy transfer in the flow covers the range between the

* Corresponding author. Tel.: +32 2 359 96 00; fax: +32 2 359 96 11.
E-mail address: nierhaus@vki.ac.be (T. Nierhaus).

0142-727X/$ - see front matter © 2007 Elsevier Inc. All rights reserved.
doi:10.1016/j.ijheatfluidflow.2007.03.005

Nomenclature

C_D [–] drag coefficient	u_τ [m/s] shear velocity
C_L [–] lift coefficient	**u** [m/s] fluid velocity
Re_b [–] bubble Reynolds number	**v** [m/s] bubble velocity
Re_τ [–] shear Reynolds number	**x** [m] bubble position
V [m^3] cell volume	α_d [–] dispersed phase volume fraction
V_b [m^3] bubble volume	γ [–] advection over rise velocity ratio
We [–] Weber number	η [m] Kolmogorov length scale
d [m] bubble diameter	ν [m^2/s] kinematic viscosity
f [N/m^3] volume specific force	ρ_c [kg/m^3] continuous phase density
g [m/s^2] gravitational acceleration	ρ_d [kg/m^3] dispersed phase density
h [m] channel half-height	σ [N/m] surface tension
L [m] length scale	ς [–] bubble spacing
p [N/m^2] pressure	τ_b [s] bubble response time
u_{bulk} [m/s] bulk velocity of the flow	τ_w [N/m^2] wall shear stress
u_r [m/s] rise velocity	Ω [–] flow domain
u_{rel} [m/s] relative velocity between the phases	$\boldsymbol{\omega}$ [1/s] fluid vorticity

system scale L and the Kolmogorov scale η, where the smallest scale eddies are dissipated into heat. However, the physics of microbubbles involves motion that lies significantly below the smallest turbulence length scales. This allows us to use simple models to take into account the presence of bubbles.

In terms of modelling the physics of two-phase flows, one can distinguish between cases where the momentum transfer from the bubbles to the carrier fluid is neglected (one-way coupling) or taken into account (two-way coupling). For very dilute flows, a one-way coupling approach is suitable. In this case, only the momentum transfer from the carrier flow to the bubbles is regarded. Back-coupling effects should be taken into account when sufficiently high concentrations of bubbles are present. In turbulent flows, it is known that the presence of bubbles can significantly influence the turbulent flow structures. For very dense flows, one has to additionally take into account collisions between bubbles. The modelling of those effects is referred to as four-way coupling. In the present work, we restrict ourselves to two-way coupled flows due to the low volume fraction of the gas phase present in our simulations.

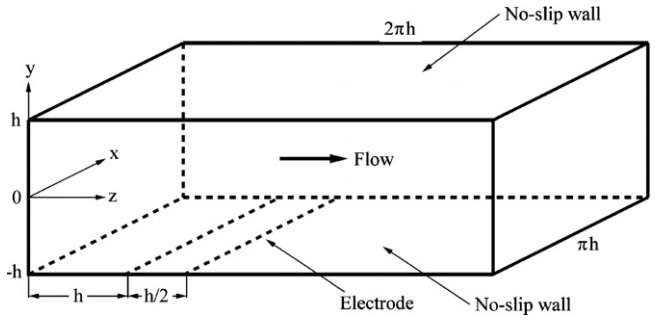

Fig. 1. Channel flow test case geometry with a gas-producing electrode located at the bottom wall.

Recent work in the frame of dispersed two-phase flow by Crowe et al. (1996) focused on collective effects of particles, droplets and bubbles, such as dispersion and evolution of local concentrations. One-way coupled bubble dispersion has been analysed numerically in publications by Wang and Maxey (1993), Maxey et al. (1994) and Giusti et al. (2005). In the latter publication, the influence of the lift force was investigated for a turbulent vertical channel flow at $Re_\tau = 150$. Two-way coupling effects have been investigated for particulate flow in a variety of numerical test cases. Solid particles in isotropic turbulence were studied by Elghobashi and Truesdell (1993) and Boivin et al. (1998), while particle-laden channel flow at shear Reynolds numbers of $Re_\tau = 85.5$ and $Re_\tau = 150$ was investigated by Pan and Banerjee (1996) and Soldati (2005). Concerning bubbly flow, the effect of two-way coupling has been studied using the two fluid formulation by Druzhinin and Elghobashi (1998, 2001), while an Eulerian–Lagrangian formulation was applied by Lain et al. (2002) and Mazzitelli et al. (2003a,b).

In the present contribution, we set aside the electrochemical part of the problem described above and model a parallel plate reactor as a turbulent channel flow of a liquid electrolyte with gas bubbles evolving from a bottom wall electrode. A simple sketch of the test case geometry is shown in Fig. 1. The channel is bounded by no-slip walls on its top and bottom, where the half-height of the channel is denoted by h. The electrode from which the gas bubbles evolve is located at the bottom of the channel and covers the entire width in the transverse direction. The periodic length of the channel in the streamwise direction is $2\pi h$ and the periodic width in the spanwise direction is πh.

We select an Eulerian–Lagrangian model to simulate the two-phase flow in the channel. Fully three-dimensional simulations of turbulent bubbly flow in a simplified model of a parallel plate electrochemical reactor are achieved by

coupling a numerical solver for Lagrangian tracking of a set of bubbles to a Navier–Stokes solver which is suitable to perform DNS. This procedure is described in detail in Section 2. Both codes used in the scope of the present work are designed to work on distributed memory parallel computer architectures.

2. Mathematical description

The modelling of bubble-laden flow is achieved by using an Eulerian–Lagrangian formulation, which describes the continuous phase by the incompressible Navier–Stokes equations, while the trajectories of the gas bubbles are tracked sequentially, each one represented by an equation of motion following Newton's second law. The phases are coupled in terms of a two-way coupling approach, where Newton's principle of reciprocal actions is realized by appropriate momentum source terms in the equations of both phases. Bubble sizes are below the smallest length scales of the turbulent carrier flow and also below the size of the smallest grid cells. For this reason, a mass-point approximation of the bubbles can be made.

2.1. Turbulent channel flow

The primary flow inside the parallel plate reactor is modelled as a turbulent channel flow between two no-slip walls, as discussed in Section 1. The fluid velocity field $\mathbf{u}$ is obtained by DNS of the incompressible Navier–Stokes equations:

$$\nabla \cdot \mathbf{u} = 0, \tag{1}$$

$$\frac{\partial \mathbf{u}}{\partial t} + (\mathbf{u} \cdot \nabla)\mathbf{u} + \frac{1}{\rho_c}\nabla p - \nu \nabla^2 \mathbf{u} = \frac{1}{\rho_c}\mathbf{f}. \tag{2}$$

Here, ρ_c is the density of the continuous fluid phase, ν is the kinematic viscosity of the fluid, p is the pressure and the vector $\mathbf{f}$ contains the forces acting on the flow. It can be decomposed into a large scale forcing term $\mathbf{f_f}$ and a force $\mathbf{f_d}$ due to momentum transfer from the dispersed phase. A description of the latter term will be given in Section 2.3. No-slip boundary conditions are applied at the channel top and bottom walls, while periodic boundary conditions are used in the streamwise and spanwise directions. We use the shear velocity u_τ and the length scale $y^+ = y u_\tau/\nu$ as characteristic scales to describe the turbulent flow of the continuous phase. The shear velocity is defined by

$$u_\tau = \sqrt{\frac{\tau_w}{\rho_c}}, \tag{3}$$

where τ_w is the average wall shear stress. The shear Reynolds number is defined as

$$Re_\tau = \frac{h \cdot u_\tau}{\nu} \tag{4}$$

and was forced to equal $Re_\tau = 131$ in the present calculations. The numerical framework used for the channel flow simulations is a spectral/finite element code, described by Snyder and Degrez (2003). The Navier–Stokes equations are discretized in x–y-planes using P1 linear finite elements, while the transverse z-direction of the flow field is represented by means of a truncated Fourier series, assuming periodicity in this direction. In this procedure, Eqs. (1) and (2) are discretized in time in a second order accurate manner. The Crank–Nicholson scheme is used to integrate the pressure and viscous terms in time, while the Adams–Bashforth method is used for the convective terms:

$$R_C^{n+1} = \nabla \cdot (\mathbf{u}^{n+1}) = 0, \tag{5}$$

$$R_M^{n+1} = \frac{1}{\Delta t}(\mathbf{u}^{n+1} - \mathbf{u}^n) + \frac{3}{2}((\mathbf{u} \cdot \nabla)\mathbf{u})^n - \frac{1}{2}((\mathbf{u} \cdot \nabla)\mathbf{u})^{n-1} + \frac{1}{\rho_c}\nabla p^{n+\frac{1}{2}} - \nu \nabla^2(\mathbf{u}^{n+1} + \mathbf{u}^n) - \frac{1}{\rho_c}\mathbf{f}^n = 0. \tag{6}$$

Concerning the finite element discretization of the continuity equation, the well-known pressure-stabilized Petrov–Galerkin (PSPG) dissipation is used to avoid spurious pressure oscillations that are encountered when using equal order elements for pressure and velocity. To eliminate convective instabilities, a fourth order Laplacian dissipation term similar to the one used by Jameson et al. (1981) is used to stabilize the momentum equation. In this way, the spatial discretization is of second order. To eliminate the remaining z-derivatives occurring after the finite element discretization, a truncated Fourier series is used. The 3D problem in physical space is transformed into a series of loosely coupled 2D problems in Fourier space by means of an FFT. For reasons of computational efficiency, the convective terms are computed in physical space and then transformed to Fourier space, which makes it a pseudo-spectral approach. The 2D linear problems are solved sequentially on a distributed memory parallel computer (Vanden Abeele et al., 2004). Inter-process communication is realized through standard MPI operations.

2.2. Lagrangian tracking of bubbles

The motion of a bubble in a turbulent carrier fluid is determined by the body and surface forces acting on it. We can define the bubble Weber and Reynolds numbers as

$$We = \frac{\rho_c(\mathbf{u} - \mathbf{v})^2 \cdot d}{\sigma}, \tag{7}$$

$$Re_b = \frac{|\mathbf{u} - \mathbf{v}| \cdot d}{\nu}, \tag{8}$$

where d is the diameter of the bubble, $\mathbf{v}$ is its velocity, $\mathbf{u}$ is the fluid velocity at the bubble center and σ denotes the surface tension of the bubble.

We consider all bubbles in our simulations as small, non-deformable and rigid spheres. This hypothesis holds for bubbles of very low Weber numbers ($We < 1$). It is valid for air bubbles with diameter smaller than 10^{-3} m moving in water, as explained by Giusti et al. (2005).

According to Ferrante and Elghobashi (2004), a no-slip condition can be applied at the bubble interface if the water

contains surfactants. For the present work, we consider that bubbles formed in electrochemical processes are contaminated by pollutants and have therefore applied no-slip drag. Furthermore, internal gas circulation effects of the bubbles are neglected.

At small bubble Reynolds numbers ($Re_b < 1$), viscous effects are dominant and the relative motion of the bubble in the fluid is in the Stokes regime. In the present work, we will restrict ourselves to bubble motion of low Re_b, so that turbulent wakes, which occur behind the bubbles at higher bubble Reynolds number, can be neglected (de Vries et al., 2002). We state Newton's second law as a Lagrangian equation of motion for each bubble

$$\frac{\partial \mathbf{v}}{\partial t} = \frac{3}{4}\frac{C_D}{d}\frac{\rho_c}{\rho_d}|\mathbf{u}-\mathbf{v}|(\mathbf{u}-\mathbf{v}) + 9\frac{\sqrt{\pi\nu}}{d}\frac{\rho_c}{\rho_d}\int_{t_0}^{t}\frac{\mathrm{d}(\mathbf{u}-\mathbf{v})}{\mathrm{d}t}\frac{\mathrm{d}\tau}{\sqrt{t-\tau}} + \frac{1}{2}\frac{\rho_c}{\rho_d}\left(\frac{\mathrm{D}\mathbf{u}}{\mathrm{D}t}-\frac{\mathrm{d}\mathbf{v}}{\mathrm{d}t}\right) + \frac{\rho_c}{\rho_d}\frac{\mathrm{D}\mathbf{u}}{\mathrm{D}t} + C_L\frac{\rho_c}{\rho_d}(\mathbf{u}-\mathbf{v})\times\boldsymbol{\omega} + \left(1-\frac{\rho_c}{\rho_d}\right)\mathbf{g}. \quad (9)$$

This equation corresponds to the formulation denoted by Maxey and Riley (1983). Here, ρ_d is the density of the dispersed phase and C_D and C_L are the drag and lift coefficients, respectively. The first three terms on the right hand side of the above equation are, in order of appearance, the Stokes drag force, the Basset history force and the virtual mass force. These forces are due to the unsteady Stokes flow of the fluid relative to the particle. The other forces are the force due to the fluid pressure gradient and viscous stresses, the slip–shear lift force and the forces due to gravity and buoyancy. In the lift force term, $\boldsymbol{\omega} = \nabla\times\mathbf{u}$ denotes the vorticity of the fluid. The derivative $\mathrm{d}/\mathrm{d}t$ is following the moving bubbles with respect to time, while $\mathrm{D}/\mathrm{D}t$ is the total acceleration of the fluid as seen by the bubble, evaluated at the bubble position. The vector $\mathbf{g}$ denotes the gravitational acceleration.

Following the empirical correlations for a fluid sphere, the drag coefficient for a spherical bubble can be evaluated as $C_D = 16/Re_b$ for small bubble Reynolds numbers (Lain et al., 2002). The bubble response time, which can be derived from the general definition of the response time of a spherical body in a flow

$$\tau_b = \frac{2}{3\mu_c}\frac{(2\rho_d+\rho_c)d^2}{Re_b C_D} \quad (10)$$

reduces to $\tau_b = d^2/24\nu$ in case of bubbly flow at low bubble Reynolds numbers, where the density of the gas is negligibly small compared to the density of the carrier flow medium. The lift coefficient equals $C_L = 0.5$ throughout our investigations. We neglect the influence of the Basset history force, which takes into account the time lag of the velocity profile around the bubble occurring in case of viscosity-driven acceleration, because we assume that velocity differences damp out rapidly for bubbles of small Reynolds numbers.

The Lagrangian equation of motion (9) is integrated in time using the Crank–Nicholson scheme, which provides second order accuracy in space and time. Together with the relation $\mathbf{v} = \mathrm{d}\mathbf{x}/\mathrm{d}t$ between the bubble velocity and its position, a system of six ordinary differential equations in three space dimensions is formed, which has to be solved for each bubble. Sequential tracking of all bubbles in the system is performed at each time step n of the Navier–Stokes solver. All bubble velocities $\mathbf{v}$ and positions $\mathbf{x}$ are updated and the source terms for the back-coupling to the Navier–Stokes solver are computed. The Lagrangian solver uses the mesh partitioning of the Navier–Stokes solver, to which it is coupled via standardized data interfaces. This allows to distribute the tracking of the bubbles to parallel computer partitions according to the mesh partitioning. The parallel architecture of the Lagrangian solver is realized through standard MPI communication.

2.3. Phase coupling

Two-way coupling between the continuous and the dispersed phase is taken into account through a procedure described by Boivin et al. (1998), where a contribution of the force $\mathbf{f_{d,i}}$ of all bubbles inside a control volume V_i around a grid node i is added to the fluid momentum Eq. (2) in this node

$$\mathbf{f_{d,i}} = \frac{\sum_{j=1}^{N_i} V_{b,j}\cdot\mathbf{f_{b,j}}}{V_i}. \quad (11)$$

Here, N_i is the number of bubbles in the volume unit and $V_{b,j}$ is the volume of a single bubble, which is modelled as a point source inside the continuous carrier flow field. Note that the forces $\mathbf{f}$ and $\mathbf{f_b}$ are per unit volume in order to agree with the formulation stated in Eq. (2). In two-way coupling, no interactions between bubbles are taken into account. In this way, the bubble trajectories are independent and in no way coupled to each other. This way of modelling turbulent dispersed two-phase flows gives statistically reliable results for sufficiently low volume fractions of the dispersed phase.

We investigated the effect of momentum back-coupling of the gas bubbles on the flow for the present configuration, where the volume fraction of the gas phase was far below $\alpha_d = 10^{-3}$. This study indicated that the back-coupling terms do not have a major influence on the flow patterns of the primary phase in the present case, since in all flow configurations tested throughout this study, the differences of the results between one-way ($\mathbf{f_d} = 0$) and two-way coupled flows were marginal. This leads to the conclusion that in flows at low bubble Reynolds numbers and low volume fractions, the advective transport from the primary to the secondary phase is highly dominant. If we regard the ratio of momentum between the dispersed phase and the continuous carrier phase inside a control volume V and assume the velocity difference

$\mathbf{u} - \mathbf{v}$ (i.e. the bubble Reynolds number) to be small, we end up with

$$\frac{m_d \mathbf{u}}{m_c \mathbf{v}} = \frac{\rho_d \cdot n \cdot V_b}{\rho_c (V - n \cdot V_b)} = \frac{\alpha_d}{1 - \alpha_d} \frac{\rho_d}{\rho_c}. \tag{12}$$

This value tends to zero for dilute bubbly flow, where the volume fraction of the dispersed phase α_d and the density ratio ρ_d/ρ_c are small compared to unity. This indicates negligible back-transfer of momentum from the dispersed entities to the flow, as it was observed in the present study. However, for a higher gas concentration with volume fractions above $\alpha_d = 10^{-3}$, Xu and Maxey (2002) as well as Ferrante and Elghobashi (2004) report a significant back-coupling effect of microbubbles on the flow, resulting in drag reduction in the wall-region.

Since, we assume the volume fraction of the gaseous phase to be far below the value of $\alpha_d = 10^{-3}$, the carrier phase density can be considered as unaffected by the presence of the bubbles (Lain et al., 2002). In this way, we can neglect mass coupling between the phases. Therefore, there is no density variation and no mass source term appearing in the fluid continuity Eq. (1) and the flow variables in the Navier–Stokes equations are not averaged by the volume fraction as has been done e.g. in the work of Ferrante and Elghobashi (2004, 2007), who investigated higher values for the volume fraction in an evolving turbulent boundary layer.

3. Numerical results

The behaviour of microbubbles injected from an electrode located at the bottom of a channel into a fully developed turbulent flow (see Fig. 1) was investigated numerically. We performed simulations of a fully turbulent flow with shear Reynolds numbers of $Re_\tau = 131$. The channel height was chosen to be of unity ($h = 1$ m). The carrier fluid was considered as water with a density of $\rho_c = 10^3$ kg/m^3 and a kinematic viscosity of $\nu = 1.025 \times 10^{-6}$ m^2/s. Calculations were performed on a grid consisting of $80 \times 64 \times 64$ points in the spanwise, wall-normal and streamwise direction, respectively. The grid is refined at the channel walls in the y-direction to provide a good resolution in the boundary layer, where the two last grid cells are at $0.16y^+$ and $0.66y^+$, respectively. There are seven points within $y^+ > 8$, which provides a sufficient resolution of the viscous sub-layer. Fig. 2 shows the relation of the grid cell size against channel height. In the spanwise and the flow direction, the cells are of equal spacing.

First of all, we regard the pure single-phase flow without bubbles and compare it to well-validated references to make sure that our primary phase flow field is well resolved. We compare our results for $Re_\tau = 131$ with the well-validated reference DNS results of Kim et al. (1987) for $Re_\tau = 180$ and Giusti et al. (2005) for $Re_\tau = 150$. Fig. 3 shows the flow statistics in terms of the mean streamwise velocity and the root mean square of the velocity components. It can be seen that the present results are slightly

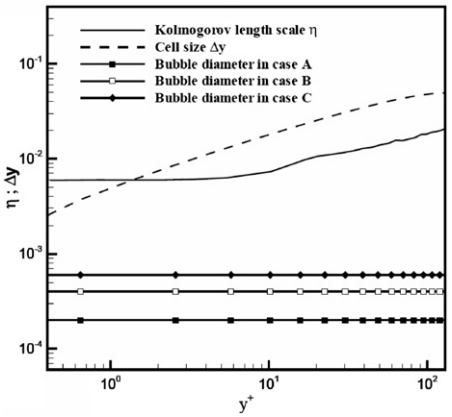

Fig. 2. Kolmogorov length scale η and grid cell size Δy as functions of the channel height in wall units.

under-resolved. For a more complete validation of the DNS solver used, the reader is referred to Vanden Abeele et al. (2004).

The bubbles that detach from the electrode are advected in the streamwise direction, while they experience a rise due to buoyancy (see Fig. 4). The bubbles were considered as air with a density of $\rho_d = 1.2$ kg/m^3. Irregular bubble dispersion and clustering effects due to turbulent fluctuations of the carrier flow are clearly visible. These phenomena will be discussed in the following paragraph. First, we introduce a dimensionless parameter γ, which represents the ratio between the bulk velocity u_{bulk} of the primary phase flow and the rise velocity u_r of a bubble:

$$\gamma = \frac{u_{bulk}}{u_r}. \tag{13}$$

The rise velocity is defined as a function of the gravitational constant g, the kinematic viscosity ν of the electrolyte flow and the bubble diameter d by the following relation:

$$u_r = \frac{g \cdot d^2}{12\nu}. \tag{14}$$

In our simulations, we choose the values of d and g in a way that the bubble Reynolds number according to Eq. (8) is kept at a constant value of $Re_b = 0.1$ and the factor γ becomes a similarity parameter, giving reasonable values in comparison with the geometry of an existing experimental reactor. This reference device is operating at an advection parameter of $\gamma_{ref} = 12$.

3.1. Bubble dispersion in a channel

We analysed dispersive effects in a two-way momentum coupled flow. The periodic boundary on the downstream side of the channel served as outlet for the gaseous phase, i.e. the bubbles were not transferred back to the corresponding upstream inlet together with the carrier flow. The flow itself, however, was subjected to a periodic

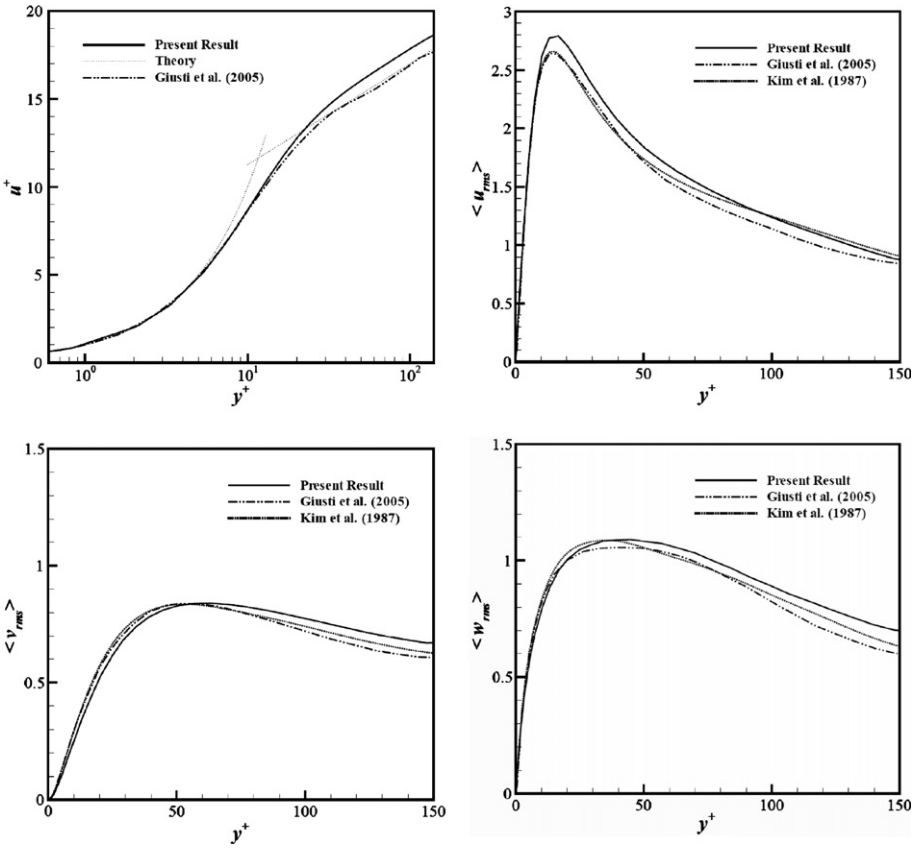

Fig. 3. Comparison between the Eulerian carrier flow statistics (mean streamwise velocity and root mean square velocity fluctuations normalized by the wall shear velocity u_τ) of the present simulation and reference data from Giusti et al. (2005) as well as from Kim et al. (1987).

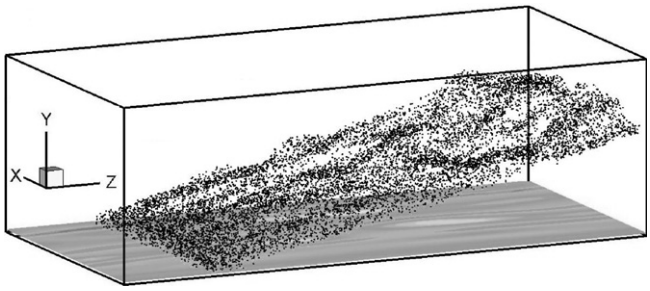

Fig. 4. Macroscopic bubble distribution in the channel and iso-surfaces of skin friction on the bottom wall.

boundary condition in this direction. Three computational runs (denoted as A, B and C) were performed, where the bubble diameter varied between 200 μm and 600 μm. From Fig. 2, we see that these bubble sizes are well below both the Kolmogorov length scale at the wall and the smallest grid element in the boundary layer. All relevant parameters for the three test cases are shown in Table 1. The bubble Reynolds number was kept at a constant value of $Re_b = 0.1$ in all computations. The bubbles were placed at random positions on the electrode, their center being a radius away from the wall. The production rate of the bubbles was 50 s^{-1}. After detaching from the electrode surface, the bubbles are advected in streamwise direction by the electrolyte due to the drag force. At the same time, they experience a rise due to buoyancy (see Fig. 4). This macroscopic motion was found to depend on the parameter γ. For an increasing value of γ, the effect of advection becomes more and more dominant. An a-posteriori calculation of the Weber number verified the assumption of rigid spherical bubbles.

We first analysed the relation between the spanwise average bubble y-position (i.e. the average height h to which the bubble has risen) and the z-position in the streamwise direction. The spanwise averaging over the width of the channel was performed according to

Table 1
Bubble diameters d normalized by the Kolmogorov length scale at the wall and the smallest cell size, bubble response times τ_b, peak volume fractions α^*_{avg} at the channel outlet, gravity scales, advection parameters and Weber numbers for comparison between test cases A, B and C

Case	d	d/η_{Wall}	d/y_1^+	τ_b	α^*_{avg}	g	γ	We
A	2×10^{-4}	0.035	0.026	1.63×10^{-3}	8×10^{-8}	0.158	3.9	0.055
B	4×10^{-4}	0.070	0.053	6.51×10^{-3}	6×10^{-7}	0.019	7.8	0.110
C	6×10^{-4}	0.105	0.079	14.6×10^{-3}	2×10^{-6}	0.006	11.7	0.165

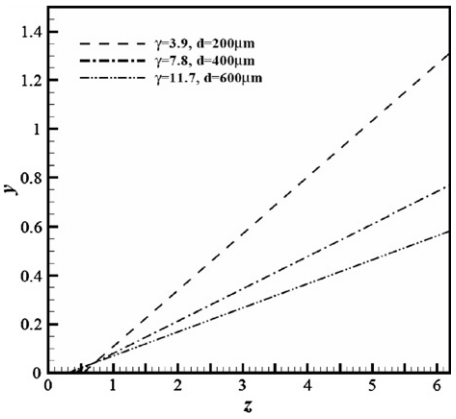

Fig. 5. Average bubble y-position as a function of the channel length z, averaged over the channel width x.

$$y_{\text{avg}} = \frac{1}{2\pi}\int_0^{2\pi} \langle y \rangle \, \mathrm{d}x. \tag{15}$$

From Fig. 5, we can see that there is an almost linear behaviour between the advection and rise velocities of a bubble. For an increasing value of γ, the influence of the advection is stronger and the angle $\beta = \arctan(y/z)$, under which the bubble rises in the streamwise direction, gets smaller.

We further computed the average gas volume fraction at the outlet of the channel ($z = 2\pi$) for all three computational runs. The average of the volume fraction was taken over time and the width of the channel by

$$\alpha_{\text{avg}} = \frac{1}{2\pi T}\int_0^{T}\int_0^{2\pi} \langle \alpha_{\text{d}} \rangle \, \mathrm{d}x \, \mathrm{d}t, \tag{16}$$

where T is the time interval of averaging. Fig. 6 shows volume fraction distributions at the channel outlet. We see that the peak volume fractions obtained are $\alpha^*_{\text{avg}} = 8 \times 10^{-8}$, $\alpha^*_{\text{avg}} = 6 \times 10^{-6}$ and $\alpha^*_{\text{avg}} = 2 \times 10^{-6}$ for the test cases A, B and C, respectively. This indicates that the initial assumption of a dilute flow was valid, because the peak values are far below the threshold of $\alpha_{\text{d}} = 10^{-3}$. If we define the bubble spacing as

$$\varsigma = \frac{L}{d} = \left(\frac{\pi}{6\alpha_{\text{d}}}\right)^{1/3}, \tag{17}$$

where L is the average distance between two bubbles, we reach a value of $\varsigma = 64.9$ for test case C, a fact that further stresses this assumption. The volume fraction in the region above the electrode, on which the bubbles are generated, reaches a peak value of $\alpha_{\text{d}} = 1.5 \times 10^{-5}$ in case C, which corresponds to $\varsigma = 32.7$. This value is also indicating a dilute bubbly flow. For volume fractions higher than $\alpha_{\text{d}} = 10^{-3}$, four-way coupling effects have to be taken into account.

From the theory of bubble interaction with turbulent flow structures it is known that bubbles tend to concentrate in regions of high vorticity (Mazzitelli et al., 2003a,b). In the present study of wall-bounded turbulent channel flow, bubbles detaching from the lower wall into the flow are found to concentrate in streamwise vortex filaments, which are created in the turbulent boundary layer. Fig. 7 shows an instantaneous horizontal crosscut of the channel at $y^+ = 32$, indicating iso-surfaces of the z-component of the vorticity and the positions of bubbles inside a section of y^+ between 29.5 and 34.5 for case C. The streamwise vortex filaments are indicated by high relative values of the z-vorticity ω_z. The alignment of the bubbles with the coherent structures is clearly visible. It was observed that the bubbles tend to cluster along the coherent structures. This effect was regarded to be most distinct in case C, where the bubble diameter, the response time and the value for γ were larger than in cases A and B. This can be related to the fact that for a higher value of γ, the effect of the gravitational rise of a bubble becomes weaker compared to the advection and it takes more time for the bubbles to vertically pass the boundary layer vortices. Thus, the bubbles have more time to align with the coherent structures than they have for low values of γ.

Figs. 8 and 9 show instantaneous vertical crosscuts of the channel at $z = 3.4$ and indicate only the lower half-height ($0 < h < 0.5$) of the channel. In Fig. 8, the instanta-

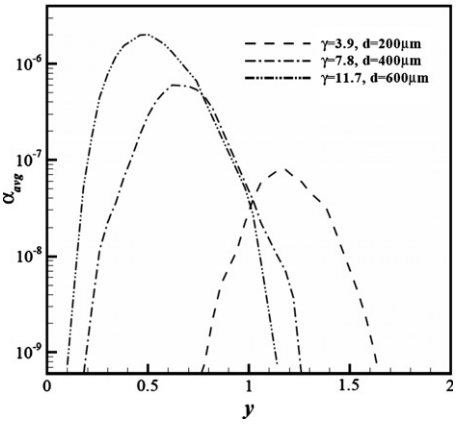

Fig. 6. Average volume fraction α_{avg} as a function of the channel height y, averaged over time and the channel width x.

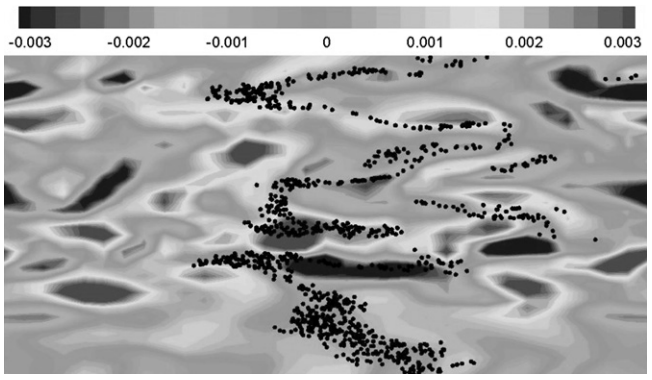

Fig. 7. Instantaneous bubble distribution and contours of ω_z in the $y^+ = 32$ plane for test case C.

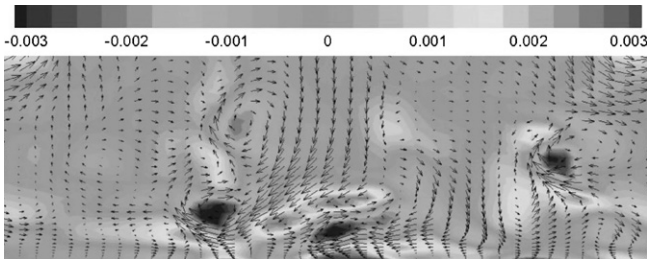

Fig. 8. Instantaneous tangent velocity vectors and contours of ω_z in the $z = 3.4$ plane for test case C.

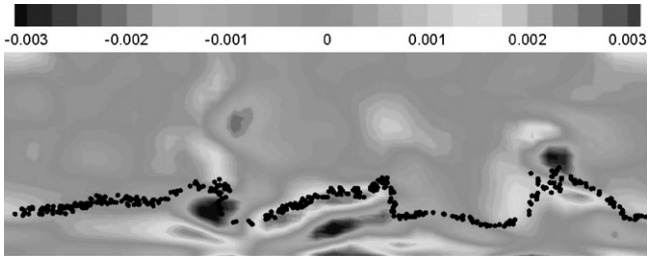

Fig. 9. Instantaneous bubble distribution and contours of ω_z in the $z = 3.4$ plane for test case C.

neous tangent velocity vectors of the primary phase flow field in the plane are shown, while Fig. 9 indicates the distribution of gas bubbles in a section of z between 3.35 and 3.45.

We can see from Fig. 9, that the bubbles are not exactly located inside the coherent vortical structures, although their motion in the spanwise and wall-normal directions seems to be highly influenced by these vortices. The bubbles are dragged towards the low-pressure regions inside the vortices by centripetal forces. This effect is due to the low density ratio between the bubbles and the electrolyte. However, this motion is superimposed by the buoyancy force. The bubbles rise vertically through the coherent vortical structures and are not fully captured inside them.

Fig. 10 shows a horizontal crosscut of the channel at $y^+ = 32$ together with iso-surfaces of the streamwise velocity component and the bubble distribution in a section of

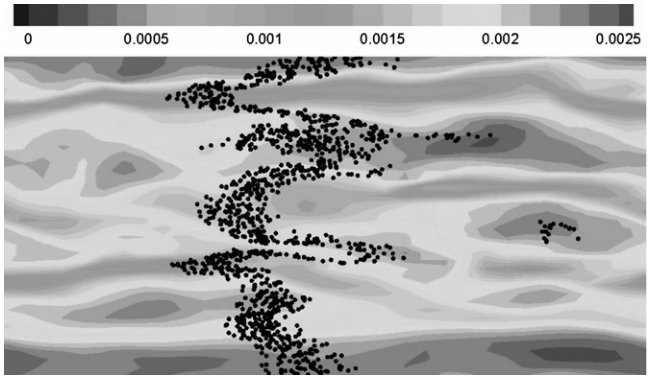

Fig. 10. Instantaneous bubble distribution and contours of the z-velocity in the $y^+ = 32$ plane for test case B.

y^+ between 29.5 and 34.5 for case B. The characteristic streamwise low-speed and high-speed streak regions of the turbulent boundary layer can be identified and the bubbles are found to align with them. The bubbles in the low-speed regions are advected less than those located in the high-speed regions. This effect can of course be related to the drag force, which acts very rapidly in case of low bubble Reynolds numbers. For a higher value of γ, this effect is even more distinct.

3.2. Effect of the lift force

According to the definition stated in Eq. (9), the slip–shear lift force depends on the instantaneous velocity difference $\mathbf{u} - \mathbf{v}$ and the fluid vorticity ω. This indicates that the effect of the lift force does not play a significant role in regions of low vorticity, but should rather be analysed for high-$\boldsymbol{\omega}$ regions in the flow.

Studies for vertical pipe flow configurations by Serizawa et al. (1975), Beyerlein et al. (1985) and Kashinsky and Randin (1999) led to the conclusion that bubbles migrate towards the channel walls in case of an upward flow, while they tend to cluster in the core of the pipe. Felton and Loth (2001) performed an experimental study of the dispersion of single bubbles in a vertical turbulent boundary layer and observed that the migration effect towards the wall is stronger for larger bubbles. Giusti et al. (2005) investigated the effect of the lift force on microbubbles in the wall-region of a turbulent upward and downward moving channel flow of $Re_\tau = 150$ and report that for this configuration, the lift force has a large effect on the behaviour of the bubble motion in the wall-region (i.e. below $y^+ = 10$) when the bubbles stay a long time in the boundary layer. For an upward flow, bubbles are pushed to the wall by the lift force, while for a downward flow, the lift force prevents the bubbles from entering the viscous sub-layer. Furthermore, is known that in the case of lift force acting on bubbles inside vortical structures, the bubbles tend to move to the downwash side of the vortex, as mentioned by Wang and Maxey (1993), Maxey et al. (1994) and Mazzitelli et al. (2003a,b), who analysed the dispersive behaviour of microbubbles in homogenous isotropic turbulence.

In the present work, we investigate the influence of the lift force on the behaviour of the bubble motion for a horizontal turbulent channel flow, where the bubbles do not stay in the wall-region for a long time due to gravitational rise. For this reason, the effect of the lift force can only be investigated in the region away from the wall in our simulations. The computations of test case C were repeated with the lift force switched off. Fig. 11 shows a streamwise vortex in a crosscut of the instantaneous flow field at $z = 4.0$ with bubble distribution in the section between $z = 3.95$ and $z = 4.05$. The black circles indicate bubble positions with included lift force ($C_L = 0.5$), while the white circles correspond to bubble positions without lift force ($C_L = 0$). The section of the crosscut containing the streamwise vortex tube is located between $y^+ = 26$ and $y^+ = 72$,

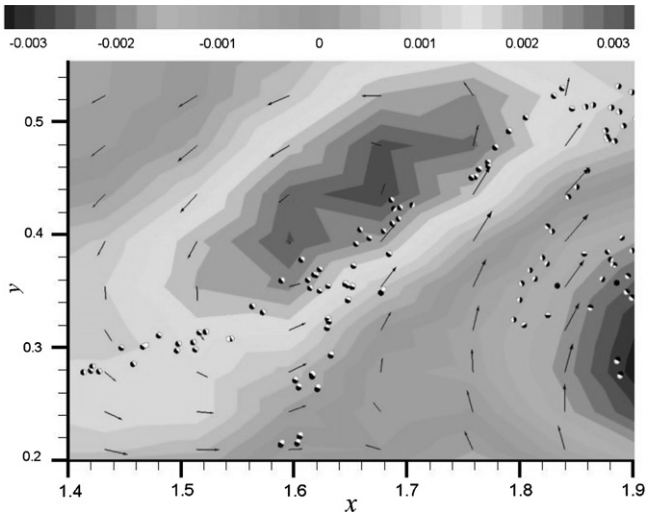

Fig. 11. Instantaneous bubble distribution and contours of ω_z in the $z = 4.0$ plane for test case C.

which is closer to the middle line of the channel than to the lower channel wall.

A close inspection of Fig. 11 reveals that the bubbles slightly move to the downwash side of the vortex when passing it under the influence of gravitational rise. This qualitatively confirms earlier observations of Mazzitelli et al. (2003b). The effect is less pronounced than in the reference article. This is mainly due to reduced gravity in our simulations (see Table 1). The average angle between the trajectories of the bubbles in the cross-cut through the vortex tube and the z-axis was 5.35°. With the lift force set to zero, it was reduced to 5.52°. The inclination angle of the bubble trajectory and thus the average bubble rise velocity are reduced by the presence of the lift force.

4. Conclusions

DNS simulations of bubble-laden turbulent channel flow were performed using a spectral/finite element based Navier–Stokes solver coupled with a Lagrangian tracking solver. Microbubbles of diameters below the Kolmogorov length scale were injected to the flow from a bottom wall electrode. All computations were performed on a distributed memory parallel computer. Two-way momentum coupling was used to simulate the interaction of the gas bubbles and the turbulent carrier flow.

It was found that the motion of the bubbles is strongly influenced by the coherent vortical structures of a turbulent boundary layer, i.e. the quasi-streamwise vortex filaments which are occurring in turbulent boundary layers. The bubbles are pulled towards the vortex centers by centripetal forces when passing these structures. However, due to buoyancy, they overcome this influence and do not stay inside the vortices.

From Figs. 7, 9 and 10, we conclude that the motion of gas bubbles lifting off from a wall electrode into a turbulent boundary layer of a channel flow involves complex kinematic phenomena, since gravitational rise, advective transport, motion due to pressure differences and the unsteady behaviour of the coherent structures are superimposed. These effects are still not fully understood and should be subject to further investigations. According to our results, the drag force and the buoyancy can be considered to be driving phenomena for dispersive effects of bubbly flow in an advection-dominated channel, where the parameter γ determines their relative importance. The effect of the lift force was found to be small. Furthermore, also the effect of momentum back-coupling from the bubbles to the flow was found to be negligible for dilute bubbly flow.

Acknowledgements

We acknowledge the support from the Instituut voor de Aanmoediging van Innovatie Soor Wetenschap and Technologie in Vlaanderen (IWT) for the MuTEch project (Contract no. SBO 040092).

References

Beyerlein, S.W., Crossmann, R.K., Richter, H.J., 1985. Prediction of bubble concentration profiles in vertical turbulent two-phase flow. Int. J. Multiphas. Flow 11, 629–641.

Boivin, M., Simonin, O., Squires, K.D., 1998. Direct numerical simulation of turbulence modulation by particles in isotropic turbulence. J. Fluid Mech. 375, 235–263.

Crowe, C.T., Troutt, T., Chung, J.N., 1996. Numerical models for two-phase turbulent flows. Ann. Rev. Fluid Mech. 28, 11–43.

de Vries, A.W.G., Biesheuvel, A., van Wijngaarden, L., 2002. Notes on the path and wake of a gas bubble rising in pure water. Int. J. Multiphas. Flow 28, 1823–1835.

Druzhinin, O.A., Elghobashi, S., 1998. Direct numerical simulations of bubble-laden turbulent flows using the two-fluid formulation. Phys. Fluids 10, 685–697.

Druzhinin, O.A., Elghobashi, S., 2001. Direct numerical simulation of a three-dimensional spatially developing bubble-laden mixing layer with two-way coupling. J. Fluid Mech. 429, 23–61.

Elghobashi, S., Truesdell, G.C., 1993. On the two-way interaction between homogenous turbulence and dispersed solid particles. Phys. Fluids A 5, 1790–1801.

Felton, K., Loth, E., 2001. Spherical bubble motion in a turbulent boundary layer. Phys. Fluids 13, 2564–2577.

Ferrante, A., Elghobashi, S., 2004. On the physical mechanisms of drag reduction in a spatially developing turbulent boundary layer laden with microbubbles. J. Fluid Mech. 503, 345–355.

Ferrante, A., Elghobashi, S., 2007. On the effects of microbubbles on Taylor–Green vortex flow. J. Fluid Mech. 572, 145–177.

Giusti, A., Lucci, F., Soldati, A., 2005. Influence of the lift force in direct numerical simulation of upward/downward turbulent channel flow laden with surfactant contaminated microbubbles. Chem. Eng. Sci. 60, 6176–6187.

Jameson, A., Schmidt, W., Turkel, E., 1981. Numerical solutions of the Euler equations by finite volume methods using Runge–Kutta time stepping schemes. In AIAA 14th Fluid and Plasma Dynamic Conference, Palo Alto.

Kashinsky, O.N., Randin, V.V., 1999. Downward liquid gas–bubbly flow in a vertical pipe. Int. J. Multiphas. Flow 25, 109–138.

Kim, J., Moin, P., Moser, R., 1987. Turbulence statistics in fully developed channel flow at low Reynolds number. J. Fluid Mech. 177, 133–166.

Lain, S., Bröder, D., Sommerfeld, M., Göz, M.F., 2002. Modelling hydrodynamics and turbulence in a bubble column using the Euler–Lagrange procedure. Int. J. Multiphas. Flow 28, 1381–1407.

Mazzitelli, I.M., Lohse, D., Toschi, F., 2003a. On the relevance of the lift force in bubbly turbulence. J. Fluid Mech. 488, 283–313.

Mazzitelli, I.M., Lohse, D., Toschi, F., 2003b. The effect of microbubbles on developed turbulence. Phys. Fluids 15, L5–L8.

Maxey, M.R., Riley, J.J., 1983. Equation of motion for a small rigid sphere in a nonuniform flow. Phys. Fluids 26, 883–889.

Maxey, M.R., Chang, E.J., Wang, L.P., 1994. Simulation of interactions between microbubbles and turbulent flows. Appl. Mech. Rev. 46, 70–74.

Pan, Y., Banerjee, S., 1996. Numerical simulation of particle interactions with turbulence. Phys. Fluids 8, 2733–2755.

Serizawa, A., Kataoka, I., Michiyoshi, I., 1975. Turbulence structure of air–water bubbly flow. Int. J. Multiphas. Flow 2, 235–246.

Snyder, D.O., Degrez, G., 2003. Large eddy simulation with complex 2D geometries under a parallel finite-element/spectral algorithm. Int. J. Numer. Meth. Fluids 41, 1119–1135.

Soldati, A., 2005. Particles turbulence interactions in boundary layers. J. Appl. Math. Mech. 85, 683–699.

Vanden Abeele, D., Degrez, G., Snyder, D.O., 2004. Parallel turbulent flow computations using a hybrid spectral/finite element method on Beowulf clusters. In: Third International Conference on Computational Fluid Dynamics, Toronto.

Wang, L.P., Maxey, M.R., 1993. The motion of microbubbles in a forced isotropic and homogenous turbulence. Appl. Sci. Res. 51, 291–296.

Xu, J., Maxey, M.R., 2002. Numerical simulation of turbulent drag reduction using micro-bubbles. J. Fluid Mech. 468, 271–281.